

Seismic interferometry as a tool for improved imaging of the heterogeneities in the body of a landfill

Konstantaki, LA; Draganov, DS; Ghose, R; Heimovaara, TJ

DOI

[10.1016/j.jappgeo.2015.08.008](https://doi.org/10.1016/j.jappgeo.2015.08.008)

Publication date

2015

Document Version

Accepted author manuscript

Published in

Journal of Applied Geophysics

Citation (APA)

Konstantaki, LA., Draganov, DS., Ghose, R., & Heimovaara, TJ. (2015). Seismic interferometry as a tool for improved imaging of the heterogeneities in the body of a landfill. *Journal of Applied Geophysics*, 122(November), 28-39. <https://doi.org/10.1016/j.jappgeo.2015.08.008>

Important note

To cite this publication, please use the final published version (if applicable). Please check the document version above.

Copyright

Other than for strictly personal use, it is not permitted to download, forward or distribute the text or part of it, without the consent of the author(s) and/or copyright holder(s), unless the work is under an open content license such as Creative Commons.

Takedown policy

Please contact us and provide details if you believe this document breaches copyrights. We will remove access to the work immediately and investigate your claim.

1 **Seismic interferometry as a tool for improved imaging of the**
2 **heterogeneities in the body of a landfill.**

3
4 **L. A. Konstantaki^a, D. Draganov^b, R. Ghose^b, T. Heimovaara^a**

5 ^aSection of Geoengineering, Dept. of Geoscience and Engineering, Delft University of
6 Technology, The Netherlands.

7 E-mail: l.a.konstantaki@tudelft.nl; t.j.heimovaara@tudelft.nl.

8 ^bSection of Applied Geophysics and Petrophysics, Dept. of Geoscience and
9 Engineering, Delft University of Technology, The Netherlands.

10 E-mail: d.s.draganov@tudelft.nl; r.ghose@tudelft.nl.

11
12 **Corresponding author:**

13 L.A. (Laura) Konstantaki

14 E-mail: l.a.konstantaki@tudelft.nl

15 Phone: +31 15 27 89132

16 Postal address: Stevinweg 1, PO-box 5048, 2628 CN Delft / 2600 GA Delft, The
17 Netherlands.

1 **ABSTRACT**

2
3 It is challenging to image and characterize the body of a landfill. High-density areas
4 that act as obstructions to fluid flow are of specific interest to the landfill operators (e.g.,
5 for improvement of treatment technologies), and thus their imaging is important. In
6 seismic reflection sections, such areas manifest themselves as sources of scattered
7 energy. The heterogeneities inside the landfill, in addition to the surface-wave energy
8 which is difficult to remove, add to the complexity in the seismic data. We propose to
9 make use of seismic interferometry (SI) as a tool to improve the imaging of the
10 scatterers, but also as a tool to remove the undesired surface-wave energy. We
11 investigate the results obtained from application of SI to field seismic reflection data
12 recorded at a landfill. We show that the data, retrieved by SI, image the scattered
13 energy better than the seismic reflection data when the latter is processed in a
14 conventional way. The increased stacking power of SI and its implicit consideration of
15 multiple scattering result in a better illumination of the scatterers. We also use SI to
16 predict the surface-wave energy and remove it from the original seismic reflection data
17 using an adaptive subtraction method. The result from the adaptive subtraction when
18 compared to the reflection data, processed in a conventional way, shows improved
19 imaging, especially of layers in the landfill. Combined interpretation of the stacked
20 reflection sections together with the velocity fields obtained from the three different
21 datasets (conventional seismic reflection, SI and adaptive subtraction) leads to an
22 improved interpretation.

23
24 **Keywords:** Landfill seismic interferometry, heterogeneity, scatterers, adaptive
25 subtraction, velocity analysis, surface waves.

1. INTRODUCTION

Using seismic interferometry (SI) it was previously shown that the imaging of near-surface (very shallow) scatterers in synthetic reflection seismic data was improved (Konstantaki et al., 2013). Compared to the data of conventional reflection seismic survey (CRSS), the results retrieved by SI were found to be less affected by errors that occur during data acquisition and processing, e.g., due to incorrect positioning of sources in time-lapse measurements or incorrect top muting. First goal of this research, is to test the previous numerical findings by applying SI to field reflection data recorded over a landfill. Both ambient-noise recordings (Campillo and Paul, 2003; Shapiro and Campillo, 2004; Draganov et al., 2007, 2009) and controlled-source recordings (Schuster, 2001; Wapenaar et al., 2002; Schuster et al., 2004) can be used in SI. Here we use controlled-source reflection recordings for SI.

In our application of SI, we cross-correlate common-receiver gathers recorded by two receivers – one at location A and another at location B – and then sum the correlation result along the sources with the aim of retrieving the reflection response at B from a virtual source at position A (e.g., Wapenaar and Fokkema, 2006; Wapenaar et al., 2010a). For a correct retrieval of the reflection response, the sources must surround the receivers. Nevertheless, it was found that even with sources and receivers only at the surface (as is the case for seismic reflection data acquisition on a landfill), the reflection response could still be retrieved (van Wijk, 2006; Halliday et al., 2007). In this case, however, non-physical arrivals might be retrieved as well (Snieder et al., 2006; Draganov et al., 2012; King and Curtis, 2012). Such non-physical arrivals would be suppressed when significant multiple scattering occurs in the subsurface (Wapenaar, 2006). In such cases, objects scattering seismic energy can be regarded as secondary (Huygens) sources that illuminate the receivers also from below.

Typically, a landfill is an extremely heterogeneous body which is full of localized objects responsible for scattered seismic energy in the reflection recordings. The presence of scattered energy in reflection data poses extra requirements to the acquisition and processing of data, thus making seismic imaging of landfills a challenging task. On the other hand, the presence of significant secondary scattering in the landfill makes the application of SI advantageous.

Backscattered or reflected body-wave seismic energy from the very near-surface objects is usually overlain by dispersive surface waves generated by an active source at the surface. Thus, an important challenge in imaging shallow scatterers through reflection seismics is the elimination of the surface waves. This is a difficult task.

1 Surface waves from other sources can also be recorded (e.g., anthropogenic traffic
2 noise or noise from gas/water pipes in the subsurface) and interfere with the active
3 recordings. More critically, the surface waves often have a similar velocity and
4 frequency content to those of the investigated signal (reflections and scattering events),
5 making it difficult to remove them by conventional methods like bandpass or frequency-
6 wavenumber (f-k) filtering (Konstantaki et al., 2015). Slightly incorrect use of the
7 parameters in the f-k filter may result in artifacts due to signal distortion and spatial
8 correlation of the background noise thus lowering further the quality of an obtained
9 image. In the synthetic data of Konstantaki et al. (2013), surface waves were not
10 present. In field data, however, surface waves are usually present, and they typically
11 obscure the imaging of the near-surface scatterers (Konstantaki et al., 2015). The
12 second goal of our study is thus to investigate the use of SI for removal of surface-
13 wave energy.

14 Prediction of surface waves with SI and their adaptive subtraction (AS) from the
15 seismic reflection data is a way to remove the surface waves. SI can be used to predict
16 surface waves without the need for a near-surface velocity model. After the prediction,
17 the surface waves retrieved by SI can be subtracted from the original reflection data
18 using an adaptive filter (Dong et al., 2006; Halliday et al., 2010). Halliday et al. (2010)
19 specifically mention the difficulties of removing scattered surface-wave energy from the
20 reflection data by conventional processing and show the advantages of AS after
21 prediction with SI. We test the use of SI to predict the unwanted surface waves and
22 remove them from the reflection data with the goal to improve the imaging of the
23 landfill.

24 Reliable characterization and imaging of the heterogeneities inside a landfill is
25 becoming increasingly important. Definition of the aftercare period, prediction of the
26 emission potential, and improvement of the treatment technologies are lately important
27 topics for the landfill operators. One of the goals is to minimize the aftercare period
28 (e.g., Scharff, 2005; van Vossen, 2010). For that purpose, a good understanding of the
29 processes occurring inside the landfill body (e.g., preferential flow paths,
30 biogeochemical processes, settlement) is essential. Many of these processes depend
31 strongly on the heterogeneity distribution inside the landfill. Konstantaki et al. (2015)
32 proposed a new approach involving CRSS and electrical resistivity methods to image
33 and characterize a landfill in detail. The third goal of this study is to investigate the
34 possibility to improve the characterization of a landfill when interpreting together the
35 results from the CRSS, SI and AS methods.

1 In the following sections, we discuss the application of SI to the CRSS data acquired at
2 a very heterogeneous landfill site. We investigate if the causal part, the acausal part, or
3 a combination of both parts of the retrieved wavefield from SI is best for the acquisition
4 geometry that we have used. We compare the result of SI with that of CRSS. Next, we
5 present the results after AS of surface waves as predicted by SI. Finally, we
6 characterize the landfill by joint interpretation of the results of CRSS, SI and AS.

7 **2. DATA ACQUISITION AND PROCESSING: CONVENTIONAL** 8 **REFLECTION SEISMIC SURVEY**

9
10 In the summer of 2013, we acquired CRSS data on a landfill in Wieringermeer, the
11 Netherlands. We used 10-Hz horizontal-component geophones as receivers and a
12 high-frequency, electrodynamic horizontal (shear-wave) vibrator as the source (Ghose
13 et al., 1996; Brouwer et al., 1997; Ghose, 2012). The horizontal geophones are
14 oriented in the crossline direction; the shear-wave vibrator is used in an SH mode,
15 which is achieved by orienting it in the crossline direction as well. In such a way, we
16 ensure that we generate and record SH waves. Compared to impulsive seismic
17 sources, high-frequency vibrators are often more suitable for resolving the
18 heterogeneities in a very heterogeneous shallow subsurface (e.g., Ghose et al., 1996;
19 Ghose et al., 1998). We have used shear (S) waves because in low-velocity soft soils S
20 waves generally offer higher resolution than P waves due to the much lower velocity for
21 S waves, and more importantly because S-wave velocity is directly linked to the elastic
22 rigidity of the subsoil and S waves are more sensitive to the subtle changes in the soil
23 type (e.g., Ghose, 2003; Ghose and Goudswaard, 2004). We used 48 geophones
24 planted along a straight line with a 0.5 m spacing between the geophones. We kept the
25 geophone array fixed and moved only the source. We shot at 33 locations, starting 4 m
26 before the first geophone and finishing 4.5 m after the last geophone using a source
27 spacing of 1 m. The noise from the nearby gas pipes and the work at nearby industrial
28 buildings resulted in a relatively low signal-to-noise (S/N) ratio in the data. Further
29 details about the acquisition parameters together with a detailed description of the
30 processing of the CRSS data can be found in Konstantaki et al. (2015).

31 The main processing steps we applied to the CRSS were as follows: (1) vibroseis
32 source-signature deconvolution to compress the raw vibrograms for each shot
33 separately in order to correct for shot-to-shot variation (Ghose, 2002); (2) vertical
34 stacking of shots at every source location; (3) bandpass filtering (4-10-160-200 Hz);
35 (4) top, bottom and surgical muting for removing the unwanted surface waves; (5)

1 iterative velocity analysis; (6) normal moveout (NMO) correction and stacking; we also
2 applied (7) prestack-depth migration.

3 **3. PROCESSING FOR SEISMIC INTERFEROMETRY**

4 **3.1 Processing steps**

5
6 To investigate if we can improve the results of CRSS at a landfill, we apply SI to the
7 CRSS data. For this purpose, we perform the following steps. First, we compensate for
8 intrinsic losses (dissipation) by multiplying the raw CRSS data by $\exp(1.3 \cdot t)$, where t is
9 time. With this, we aim to boost the later arrivals for the correlation process. Then we
10 top-mute the direct arrivals and sort the data to common-receiver gathers (CRG). After
11 that, we cross-correlate the CRGs and sum each correlation result along the sources.
12 As a final step, we apply a bandpass filter (5-35-95-110 Hz) to remove low- and high-
13 frequency noise and a notch filter to remove the 50-Hertz powerline noise. The latter
14 noise is present in the CRSS data, and the cross-correlation process amplifies it.
15 Therefore, we need to suppress it. Once the virtual common-source gathers are
16 retrieved by SI, we apply the same processing steps 4) to 6) as described in section 2.
17 To obtain stacked images of the landfill from the SI data, we use retrieved common-
18 midpoint (CMP) gathers with a CMP fold ≥ 6 . We apply post-stack automatic gain
19 correction (AGC) with a 30 ms window to the stacked images for a better visualization.
20 We finally apply a post-stack bandpass filter (10-35-95-110 Hz) to remove the low- and
21 high-frequency noise that is boosted by the correlation process. After the stacking, we
22 perform a time-to-depth conversion using a smoothed version of the stacking velocity
23 field.

24

25 **3.2 Using parts of the causal and acausal retrieved results**

26

27 Using SI by cross-correlation requires illumination from all sides. When the illumination
28 is homogeneous, physical arrivals will be retrieved equally well in the causal and
29 acausal part of the wavefield (Wapenaar, 2004; van Manen et al., 2005; Wapenaar et
30 al., 2010b). The causal part refers to times later than the zero time (positive time) and
31 the acausal part to times earlier than the zero time (negative time). In such a case, the
32 final retrieved result can be taken only from the positive times, only from the negative
33 times, or even from their summation, where the latter might result in improved S/N
34 ratio. In case when the illumination is not homogeneous from all sides (e.g., when one-
35 side illumination occurs or gaps in the illumination are present) then parts of the
36 physical energy can be retrieved at positive times and other parts at negative times.
37 Furthermore, artifacts may appear; for example, physical arrivals retrieved at negative

1 times may continue to positive times as non-physical arrivals and thus manifest
2 themselves there as artifacts. For our dataset, the illumination is not homogeneous
3 because the sources are present only at the level of the receivers instead of effectively
4 surrounding the receivers. Therefore, to retrieve more complete reflections, we take
5 parts of the positive times and/or parts of the negative times. To understand how we
6 choose which parts to use, we make a simple assumption of a horizontally layered
7 subsurface representing the landfill and a homogeneous halfspace below it (Figure 1).
8 In the figure, the location of receiver A is the position where a virtual source will be
9 retrieved, whereas location B is the receiver where we want to retrieve the reflection
10 from the bottom of the layer. Using stationary-phase principles (Snieder, 2004) it can
11 be shown that sources lying around the stationary-phase point (inside the stationary-
12 phase region) contribute constructively to the retrieval of physical energy, while arrivals
13 from sources outside this region interfere destructively. For our case with sources and
14 receivers at the surface, a reflection is retrieved by the correlation, for example, of a
15 primary reflection with its first-order free-surface multiple. The correlation process
16 would subtract the traveltimes of the primary from that of the multiple, resulting in the
17 retrieval of a physical primary reflection between A and B. For the case in Figure 1 with
18 a homogeneous horizontal layer, the stationary-phase point will be at a distance AB to
19 the left of A or to the right of B. For a virtual source at A and a receiver at B, the
20 reflection will be retrieved at positive times when the sources are located to the left of A
21 (Figure 1a). Similarly, the reflection will be retrieved at negative times when all sources
22 are present to the right of B (Figure 1b). Having a heterogeneous subsurface with
23 scatterers will complicate the situation. In that case, such a simple analysis is not
24 necessarily correct. The presence of scatterers in the subsurface partly helps to
25 overcome one-side illumination as the scatterers act as secondary (Huygens) sources
26 and energy is scattered back to the surface (e.g., Konstantaki et al., 2013).
27 Nevertheless, the number and location of scatterers in the subsurface is unknown on
28 beforehand and, hence, we do not know whether the secondary illumination would be
29 sufficient to result in retrieval of physical arrival both at positive and negative times. If a
30 physical arrival is retrieved only, for example, at positive times for a certain retrieved
31 trace, summing to the positive times the retrieved negative times would not add extra
32 information. For this reason, we inspect how the retrieved results look like for a number
33 of virtual common-source gathers for positive times, negative times, summed times or
34 a combination of all (mixed-traces approach).
35

1 From inspection, we conclude that for our field dataset we can decide which times
2 (positive, negative or summed) to be used for each trace depending on the relative
3 position of A, B, and the majority of sources. Instead of choosing the times for each
4 trace of each virtual common-source gather separately, we make this procedure
5 automatic. The general rule that we have applied is that we take positive times in case
6 A is between B and the majority of sources and we take negative times when B is
7 between A and the majority of sources. In order to make this distinction, we should
8 have at least 2/3 of the sources on one side of A or B. With a total of 33 sources, it
9 means that at least 22 sources must be on one side in order to consider them as
10 acceptable majority. If that is not the case, then we take the summation of the retrieved
11 positive and negative times to increase the S/N ratio. When A and B coincide, we take
12 only the positive times. We can summarize this as follows:

13

$$14 \text{ trace} = \begin{cases} \text{Positive time, if } q \geq 22 \text{ with } x^s < x^A < x^B, \text{ or } x^s > x^A > x^B, \text{ or } x^A = x^B \\ \text{Negative time, if } q \geq 22 \text{ with } x^s < x^B < x^A, \text{ or } x^s > x^B > x^A \\ \text{Sum of positive and negative time, if } q < 22 \end{cases},$$

15

16 where x^s indicates the position of the sources, q is number of sources, x^A is the
17 position of A and x^B is the position of B. A comparison among the SI mixed-traces
18 approach (SI^M), the result when only the positive times are used (SI⁺), the result when
19 only the negative times are used (SI⁻), and the CRSS data is shown in Figure 2. We
20 choose the shot location at horizontal distance 7 m because it has a mixture of positive,
21 negative and summed traces. The green rectangle shows the area of improvement in
22 SI^M compared to SI⁺. In the SI⁺ result, the area enclosed by the green rectangle is ringy
23 and events are difficult to interpret. Due to the ringy nature, the retrieved artifacts might
24 be interpreted as scattering arrivals (e.g., the orange hyperbola). Retrieved artifacts are
25 a result of non-homogeneous illumination. The artifact indicated with the orange
26 hyperbola is a non-physical arrival due to insufficient illumination from the sources to
27 the left of the virtual-receiver positions. We see here that the secondary scattering was
28 not sufficient to overcome the problem of one-side illumination. To retrieve physical
29 arrivals in this area, sources on the right side of the receiver locations must be used,
30 which then corresponds to events retrieved at negative times (and/or summed times as
31 explained in the equation above). Comparing SI^M with CRSS, we notice similarities
32 between the events that are not clear in SI⁺ (grey-shaded areas).

33 The red rectangles show the improvement in SI^M over SI⁻. Note, for example, the
34 retrieved events inside the right red rectangle which appear to propagate to the virtual

1 source. These are retrieved artifacts due to a lack of retrieved physical energy at that
2 part of the negative times. The illumination from the sources located on the right of the
3 virtual-receiver locations is insufficient. To retrieve physical arrivals in this area,
4 sources on the left side of the receiver locations must be used, which then corresponds
5 to events retrieved at positive times (and/or summed times as explained in the equation
6 above). The grey-shaded areas and hyperbolas show a comparison between the three
7 different SI results and the CRSS result for the reflections and the scattering events,
8 respectively. The improvement of SI^M over SI^+ and over SI^- is clear – the events are
9 more coherent and better identifiable in SI^M . The presence of sufficient scatterers might
10 help to homogenize the illumination of the receivers from the active sources, and thus
11 result in more comparable positive and negative times. For our data, we see that such
12 homogenization is not the case due to the insufficient number of scatterers and the
13 presence of intrinsic losses. Therefore, we need to use the mixed-traces approach.
14 The stacked sections from CRSS, SI^M , SI^+ and SI^- data (Figure 3) confirm our previous
15 conclusions. Once again the rectangles mark the areas of improvement in the SI^M
16 result compared to SI^+ and SI^- results, and the grey-shaded areas and hyperbolas mark
17 the imaged scatterers to which the marked events shown in Figure 2 have contributed.
18 In general, the events are more coherent in SI^M . They show more clarity and are in
19 agreement with the CRSS result. The artifact highlighted by the orange hyperbola
20 appears as a scatterer in the SI^+ result, whereas in the SI^M it can be interpreted as a
21 linear event, similar to that in CRSS. In the red area marked in the SI^- result, it is visible
22 that the S/N ratio is lower in SI^- than in SI^M . Because of these, from now onwards we
23 will use only the SI^M result, but for simplicity we will call it just SI. Note that the ringing
24 that appears in the lower left corner of the stacked images is an artifact of the post-
25 stack bandpass filter. In Figures 3e-h we show enlarged areas from the stacks in
26 Figures 3a-d, respectively, for better visualization of the scatterers.

27 **4. IMAGING SCATTERERS WITH SEISMIC INTERFEROMETRY**

28 **4.1 Comparison of the results of SI and CRSS**

29
30 Figure 4 presents an example of CRSS and SI common-source gather for a source at
31 horizontal location 22 m. We show both raw (Figures 4a and 4c) and processed data
32 (Figures 4b and 4d). We choose the common-source gather for a source at distance 22
33 m (thus different from the one in Figure 2), because both reflections and scattering
34 events are easily interpretable here. Another reason is that we will subsequently use
35 this shot gather in explaining AS for suppression of surface waves. The shot gathers in
36 Figures 4b and 4d are obtained after application of the processing steps as explained

1 in section 2. The grey-shaded areas indicate interpreted reflections. Ideally, these
2 events should be at the same position in all these plots. The red hyperbolas mark those
3 scattering arrivals which we can identify on the CRSS shot gathers (Konstantaki et al.,
4 2015), whereas the green hyperbolas mark the ones which we can interpret
5 unambiguously only on the SI shot gathers and not on the CRSS shot gathers. As the
6 CRSS data are obtained by deconvolution and the SI data by cross-correlation, both
7 CRSS and SI data show traces with zero-phase wavelets. Scattering events 1 and 2
8 interpreted in the CRSS shot gather are also interpretable in the SI shot gather, though
9 not equally clear. Scattering events 5 and 6 appear strongly in the SI data. There is a
10 hint of their presence also in the CRSS gather, but there they are not unambiguous.
11 Scattering events 3 and 4 apparently exhibit opposite polarities on the CRSS and SI
12 gathers. This will be explained later on in section 4.2. The reflections are interpretable
13 in both datasets, but in the SI gather they appear more continuous and coherent.
14 Figure 5 shows the stacked images obtained from the CRSS and SI datasets.
15 Concentrating on Figures 5a and 5b, we can identify specific structures. Both sections
16 show predominance of laterally continuous reflections on the right part (18 m to 26.25
17 m horizontal distance). A dome-like structure appears in the middle (approximately 13
18 m to 17 m horizontal distance), which is more prominent in the SI section. We shall
19 explain this event further in the Discussion section, after having interpreted the results
20 of the AS approach.
21 Looking carefully at the events in the SI and CRSS stacked sections, it is clear that
22 more scatterers can be interpreted in the SI section. The interpreted scatterers are
23 marked in Figures 5c and 5d. In Figures 5e-h we show enlarged areas from the stacks
24 in Figures 5a-d, respectively, for better visualization of the scatterers. In accordance
25 with the interpretations in the common-source gathers, the green colour indicates
26 scatterers that can be interpreted only in the SI section but not in the CRSS section,
27 whereas the red colour indicates scatterers that can be interpreted in the CRSS result.
28 The blue arrows point to reflectors. The reflectors seen in the SI stacked section are
29 interrupted by scatterers (e.g., scattering events 5 and 6 in Figure 5d), while in the
30 CRSS section we do not see such interruption. The higher number of traces in the SI
31 data has made it possible to distinguish these extra scatterers (Konstantaki et al.,
32 2013). This will be further explained in section 4.3.
33 Shallow scatterers (e.g., green hyperbolas at a horizontal distance of about 9.25 m and
34 14.25 m, and two-way traveltimes (TWT) 25 ms and 30 ms, respectively) can be
35 identified in the SI stacked section (Figure 5). In the CRSS section, these events are
36 not interpretable, most likely because they were muted out in the preprocessing. In our

1 case, the SI data utilizes secondary scattering in order to retrieve the energy from the
2 shallow scatterers and thus remedies the problem posed by muting in the CRSS data
3 (Konstantaki et al., 2013).

4 5 **4.2 Modelling study 1: Opposite-polarity effect**

6
7 In Figure 5, we identify some events that exhibit opposite polarities between CRSS and
8 SI stacked sections, similar to what we see in the shots gathers in Figure 4 (e.g.,
9 scattering events 3 and 4). Note that in the two stacked sections, scatterers 3 and 4 do
10 not appear at the same location, although this was not apparent in the shot gathers in
11 Figure 4. Concentrating on the events shown in the small yellow rectangles in Figure 5,
12 we notice clearly the opposite-polarity effect: what appears to be a peak in the CRSS
13 section (the red hyperbolas in the yellow rectangles in Figure 5c) shows up as a trough
14 in the SI section (the red hyperbolas in the yellow rectangles in Figure 5d). A peak
15 appears at an earlier time in the SI section (the green hyperbolas in the yellow
16 rectangles in Figure 5d). These red- and green-marked events correspond to the same
17 scatterer. We use Figure 6 to explain this effect. In Figure 6a the green hyperbola
18 indicates a reflection event and the dashed green line is the same event after NMO
19 correction. The blue hyperbola indicates a diffraction event and the dashed blue
20 hyperbola is the alignment of the diffraction event after time-shifting using the root-
21 mean-square (RMS) velocity of the reflection event for NMO correction. For velocity
22 analysis, we use the stacking velocity corresponding to the main layer boundaries. The
23 moveout velocity in this example is 90 m/s for the reflection and 60 m/s for the
24 diffraction. When the reflection velocity field is used, the diffraction event is not
25 flattened after the NMO correction (Figure 6a). This is true for both CRSS (Figure 6b)
26 and SI (Figure 6c) data. However, as the SI data contain a larger number of traces
27 (denser spatial sampling), it images the position of the scatterer more accurately. This
28 can be interpreted as an aliasing effect in the CRSS result (due to spatial
29 undersampling). As shown in Figure 6f, the stacked trace from the SI data provides a
30 more correct time for the apex of the scatterer, compared to the stacked trace in the
31 CRSS section (Figure 6e). In the CRSS stacked trace, we lose the information close
32 to the apex and the scatterer appears at a later time. A comparison between the
33 stacked traces shows a different waveform for the CRSS and SI result that could be
34 interpreted as the opposite-polarity effect (grey arrows in Figure 6d), similar to what we
35 observe in the field data (Figure 5).

36 37 **4.3 Modelling study 2: Scatterers located at layer boundaries**

1
2 To understand why the SI result could reveal scatterers that overlay reflectors, we
3 perform a modelling study. We use a model consisting of four horizontal layers with two
4 scatterers placed on the boundary between the two top layers (Figure 7a). The shear-
5 wave velocity (V_s) and density (ρ) of the layers are: Layer 1: $V_s=82$ m/s, $\rho=800$ kg/m³;
6 Layer 2: $V_s=100$ m/s, $\rho=810$ kg/m³; Layer 3: $V_s=120$ m/s, $\rho=820$ kg/m³; Layer 4: $V_s=140$
7 m/s, $\rho=840$ kg/m³. Both scatterers are 1 m wide, 0.3 m high and have $V_s=140$ m/s and
8 $\rho=900$ kg/m³. The separation between the scatterers is 3 m. We consider the same
9 acquisition geometry as we have in the field to generate synthetic data: 33 sources with
10 1 m spacing and 48 receivers with 0.5 m spacing. The first source is located at 134 m
11 and the last source at 166 m, whereas the first receiver is located at 138 m and the last
12 at 161.5 m. The scatterers are located at horizontal positions 148 m and 152 m. The
13 grid sampling in the model is 0.09 m and the time sampling of the receiver field is 0.003
14 s. We apply a taper of 60 points at the lower and side boundaries of the model to
15 minimize reflections from these boundaries. We perform forward modelling using a
16 finite-difference code (Thorbecke and Draganov, 2011) in acoustic mode but with S-
17 wave velocity parameters. This is justified, because in the field we generated and
18 recorded SH waves, which decouple from the P and SV waves in a 2D experiment. To
19 model SH-wave propagation assuming decoupling, one can thus use a simple acoustic
20 forward modelling with S-wave velocities.

21 Figure 7b shows the stacked section obtained from the modelled CRSS data. Figure 7c
22 shows the stacked section obtained from the retrieved common-source gathers after
23 applying SI to the modelled CRSS data. In the stacking process, we use the RMS
24 velocity field obtained from the exact velocity model. In the SI section, two clear bumps
25 are visible at the first layer boundary with apex at the correct scatterer locations. In
26 contrast, in the CRSS section the apex of the scatterers is not clear and the
27 interpretation of the location of the scatterers is difficult because of the presence of
28 large and strong diffraction smiles. If more scatterers were present (as in our field
29 data), it would be difficult to distinguish the scatterers located at the layer boundary in
30 the CRSS section. The diffraction smiles are nearly absent in the SI stacked section
31 due to the improvement in stacking due to the increased fold of the traces to be
32 stacked, because of more available sources and receivers. The top three layers are
33 visible in both CRSS and SI sections. In the SI section, the layers are imaged well,
34 except at the extremities of the receiver array. On the contrary, in the CRSS section the
35 layers are clearly interpretable only at extremities of the receiver array where there is
36 no interference due to the diffraction smiles. In the SI stacked section, the imaging of

1 reflections at the sides is poor due to insufficient stacking; the CMP fold is lower than
2 that for the CRSS data. Note that the deepest reflector is not imaged in the SI data,
3 because reflections from this boundary are not retrieved. This happens due to the
4 length of the modelled data, which was sufficient to record the primary reflection from
5 the fourth layer, but too short to record its free-surface multiples.

6 7 **4.4 Remarks on the comparison of SI and CRSS results**

8
9 From the comparison of CRSS and SI results in this section, the following remarks can
10 be made:

- 11 • In the SI stacked section, scatterers appear at a time which is more likely to be
12 the correct one, due to more available traces in the CMP gathers compared to
13 the CRSS stacked section;
- 14 • Scatterers located at or close to a layer boundary are better imaged through SI;
- 15 • Shallow scatterers that are muted in the CRSS data can still be imaged in the
16 SI stacked section.

17 However, as we found in our earlier modelling (Konstantaki et al., 2013), artifacts are
18 also expected in the SI results. Therefore, a joint interpretation of CRSS and SI results
19 is desirable in order to interpret correctly the scatterers.

20 **5. REMOVING SURFACE WAVES USING SEISMIC** 21 **INTERFEROMETRY: IMPROVED IMAGING OF THE REFLECTORS IN** 22 **A LANDFILL**

23 **5.1 Preparation of data for adaptive subtraction**

24
25 Surface waves with velocity and frequency similar to those of the reflections and the
26 scattering events are present in our field data and it is challenging to remove them
27 through data processing. In the processing of CRSS data we remove the surface
28 waves by surgical muting. This does not remove the surface-wave energy in a
29 satisfactory manner, because the surface-wave energy that overlaps the useful
30 reflection and scattered arrivals still stays. Furthermore, weak reflections and scattered
31 arrivals covered by surface waves can also be muted.

32 Here, we use SI as a tool to remove in a data-driven way the surface-wave energy from
33 the shallow reflection data. For this purpose, we subtract the surface waves in an
34 adaptive manner. To remove the surface waves from the CRSS data, first we need to
35 predict the surface waves by retrieving them with SI. We first compensate for the
36 intrinsic loss by multiplying the CRSS data with $\exp(1.3 \cdot t)$. Then, we apply a bandreject

1 filter (5-35-95-110 Hz) followed by top muting of the direct arrivals in order to enhance
2 the surface waves. Note that we now apply a bandreject filter to reject frequencies that
3 were kept before (those characteristic of reflections and diffractions) and boost low and
4 high-frequency surface waves (that were rejected during the SI and CRSS processing).
5 After that, we apply SI using the mixed-traces approach as explained in section 3. The
6 result is SI data with dominant surface waves (SI^S).

7 An example of this retrieval in field data is illustrated in Figure 8b. For a comparison,
8 the CRSS shot gather at the same location (shot at 22 m horizontal distance) is shown
9 in Figure 8a. Next, we use a least-squares matching filter that minimizes the difference
10 between the CRSS and the SI^S data (Verschuur et al., 1992; Guitton and Verschuur,
11 2004). For our data, we found that the best matching is achieved when we use a filter
12 with a length of 21 sample points, a time window of 100 sample points, and a spatial
13 window of 5 traces. Using this filter, the SI^S data (Figure 8b) are adaptively subtracted
14 from the CRSS data (Figure 8a). The resulting AS data is shown in Figure 8c.

15

16 **5.2 Comparison of the results of CRSS and AS**

17

18 Comparing the gathers in Figures 8a and 8c, we see that surface-wave energy is
19 significantly removed, and at many places the reflections are better identifiable in the
20 AS shot gather. Refractions, now free from surface-wave energy, are also better
21 visible. In Figure 8b, the SI^S shot gather shows an event at about 16 m horizontal
22 distance and TWT of 0 ms, which looks like a surface wave from another source. This
23 event is also present in the CRSS data and becomes clearly visible when the same
24 bandpass filter is applied. Figures 9a and 9b show the shot gathers from Figures 8a
25 and 8c, respectively, after top and bottom muting. We apply the same top and bottom
26 mute in both shot gathers. The application of SI followed by AS suppresses very
27 effectively the surface waves at later times. In our case, for imaging the landfill using
28 shear waves, we are mainly interested in the first 180 to 200 ms (which corresponds to
29 approximately 11 to 13 m depth where we expect the bottom of the landfill). Therefore,
30 for comparison, we apply the same bottom mute as that for the CRSS data. Note that
31 in the AS data we do not apply surgical mute to all shot gathers for surface-wave
32 removal - only a few shot gathers show remaining strong surface waves that need to
33 be removed by surgical muting. This is because the AS filter parameters are not ideal
34 for all shot gathers and in a number of shot gathers a few surface waves are still
35 present. The grey-shaded areas in Figures 9a and 9b highlight reflections from layer
36 boundaries. The red hyperbolas highlight the scattering events interpreted on the
37 CRSS data (Figures 4a and 9a), whereas the green hyperbolas are the scattering

1 events interpreted on the SI data (Figure 4d). The reflections (grey-shaded areas) are
2 identifiable in the AS result – some of them are even more continuous and laterally
3 coherent. The scattering events are not improved after AS, but this is also not
4 expected. The quality of the scatterers might even have deteriorated.

5 During the SI processing, surface waves between a virtual source and a receiver are
6 retrieved for each of the active-source positions, over which the summation takes
7 place. This results in a retrieval of relatively strong surface waves. A reflection between
8 the same virtual source and a receiver will be retrieved only for a few sources, which lie
9 in the stationary-phase region. Because of this, the retrieved reflections will be
10 relatively weak unless a large number of sources are available. Scattered arrivals
11 between the virtual sources and the receiver might also be retrieved for each active-
12 source position, but that will depend on the recording time and the path of the scattered
13 wave in the CRSS data. Because of this, a retrieved scattering will be relatively
14 stronger than a retrieved reflection, but relatively weaker than a retrieved surface wave.
15 In the AS, the strongest arrivals, i.e. the surface waves, will dictate the parameters of
16 the matched filter and thus the surface waves will be most effectively removed. The
17 weaker arrivals, like the scattering, might also be affected, but to a lesser extent. How
18 much of the scattered energy is preserved after the AS would depend on how much
19 surface-wave energy is retrieved and the difference in amplitude between the surface
20 waves and the scattered arrivals.

21 Figure 10 shows the stacked sections from the CRSS and AS data. Note that in the AS
22 section the reflectors are clearer. The interpretations are marked in Figures 10c and
23 10d. The grey-shaded areas highlight the reflectors. The reflectors on the right and left
24 sides (18 m to 26.25 m and 5.25 m to 8 m horizontal distance, respectively) are more
25 continuous in the AS result. On the other hand, between about 12 m and 15 m
26 horizontal distance, TWT of 140 ms the reflectors appear to be more continuous in the
27 CRSS data. The reason for this is likely to be the surface-wave energy that was not
28 removed in the AS data, but was removed in the CRSS data by surgical muting. Note
29 that the AS section allows much better identification of the bottom of the landfill (yellow
30 line in Figure 10d).

31 As discussed earlier, the scatterers in the AS section in Figure 10 are not always well-
32 imaged as compared with the CRSS section. The scatterers highlighted with red
33 hyperbolas are imaged satisfactorily, although not always at the same location as in the
34 CRSS data. The green-highlighted scatterers are difficult to interpret.

35 Ideally, SI can be applied to the AS data to improve the retrieval of scattering events
36 compared to the original SI data (SI applied directly to the CRSS), since the

1 interference from surface-wave energy would be less in case of the AS data. However,
2 our field data have a low S/N, implying that SI applied to the CRSS data would also
3 result in a low S/N and consequently the AS result has a lower S/N. The application of
4 SI on the result of AS would be even worse. To improve the retrieval of the scattered
5 arrivals, one needs to have longer AS data. If the noise in the field data can be reduced
6 through more careful data acquisition, then that will help the situation greatly.

7 **6. CHARACTERIZATION**

8
9 For a reliable estimation of the emission potential of a landfill, determination of the
10 detailed density distribution is important (White et al., 2004; McDougall and Fleming,
11 2013). Konstantaki et al. (2015) translated the velocity field obtained from CRSS data
12 to density distribution using a tested empirical relationship that is specifically valid for
13 landfill sites. Errors in the velocity models, however, significantly influence the
14 characterization of the landfill properties (e.g., Zhu et al., 1998). Therefore, the
15 extracted velocity field needs to be reliable.

16 As we have shown above, CRSS may fail to image certain scatterers and reflectors,
17 whereas using SI one might improve the imaging of the shallow subsurface. However,
18 SI might also create artifacts. Therefore, a combined interpretation of the velocity fields
19 obtained from CRSS, SI and AS might lead to a more reliable characterization of the
20 shallow subsurface.

21 For all three datasets (CRSS, SI and AS), we estimate the RMS velocities by
22 interactive velocity analysis. For this, we follow the procedure specifically valid for a
23 very heterogeneous subsurface condition like in landfills, as explained in Konstantaki et
24 al. (2015). This requires special care. Using the Dix equation, we then convert the RMS
25 velocities to interval velocities. Figures 11a,b,c illustrate the estimated velocity field
26 obtained from the CRSS, SI, and AS data, respectively. The circles in Figure 11 mark
27 areas showing clear differences among the three velocity fields. The SI data present a
28 more heterogeneous velocity field compared to the AS data. This is anticipated
29 because SI illuminates multitude of localized scatterers in the landfill. On the other
30 hand, the AS velocity field is smoother, because of the predominance of reflections
31 from layer boundaries rather than from spatially localized scatterers. The differences
32 between the three velocity fields appear meaningful.

33 These differences can be explained based on the events that each dataset (CRSS, SI
34 and AS) images. We present a few examples here. In the CRSS data in Figure 5c, a
35 scatterer is imaged at about 8.5 m horizontal distance and TWT of 150 ms (red

1 hyperbola). This scatterer appears in the CMP gathers, and during the velocity
2 analysis, velocity was picked such that this scatterer is imaged best (Konstantaki et al.,
3 2015). For this reason, a high-velocity anomaly compared to the surrounding appears
4 at this location (marked by A in Figure 11a). On the other hand, in the SI data, not one
5 but two scatterers are imaged in this vicinity (Figure 5d): 8.75 m horizontal distance
6 and TWT of 130 ms, and 9.25 m horizontal distance and TWT of 100 ms (green
7 hyperbolas), although no scatterer is imaged at exactly the same location marked by
8 the red hyperbola (scatterer in the CRSS data). This is the reason why we notice in the
9 SI velocity field two spatially resolved high-velocity localities (marked by two circles
10 close to A). At location B, a lower velocity appears in the SI velocity field compared to
11 the CRSS velocity field. This is because a scatterer is imaged at this location in the SI
12 data (see the SI stacked section in Figure 5d at 9.25 m horizontal distance and TWT of
13 25 ms), but not in the CRSS data (Figure 5c). Next, the velocity contrast at location C
14 appears at different times between Figures 11a and 11b, because of the opposite-
15 polarity effect. As discussed in section 4.2, the scatterer at around 16 m horizontal
16 distance in the CRSS stacked section (Figure 5c yellow rectangle, red hyperbola)
17 appears at a later time than that in the SI stacked section (Figure 5d yellow rectangle,
18 green hyperbola). Because of this, we find the velocity contrast appearing at a later
19 time in the SI velocity field (Figure 11b) compared to the CRSS velocity field (Figure
20 11a). SI fails to image the scatterer located at about 25.75 m horizontal distance and
21 TWT of 150 ms (Figure 5d), which is though clearly visible in the CRSS data (Figure
22 5c). This explains the presence of a clear anomaly at this location in the CRSS velocity
23 field and its absence in the SI velocity field (circle D).

24 Compared to the CRSS and SI velocity fields, the AS velocity field is generally rather
25 smooth (dominated by reflections from the layer boundaries rather than by the
26 scatterers). Nevertheless, a few localized velocity contrasts can be traced in Figure
27 11c. As discussed earlier, several scatterers are still picked in the AS data during
28 velocity analysis, and they are imaged in the AS stacked section. We, therefore, still
29 observe some spatially localized velocity anomalies in Figure 11c. Circle A in this figure
30 indicates a localized scatterer in this area (corresponds to the one at 8.5 m to 9.25 m
31 horizontal distance and TWT of 100 ms to 150 ms in Figure 10d). Similarly, circle C in
32 Figure 11c indicates the velocity anomaly due to scatterers at approximately 16 m
33 distance and TWT of 100 ms and 130 ms (Figure 10d). Admittedly, in the AS stacked
34 section, due to the lower S/N, the imaged scatterers are sometimes less unambiguous,
35 as explained in the previous section. Therefore, one needs to be cautious in
36 interpreting the localized anomalies in the AS velocity field.

1 7. DISCUSSION

2
3 In the SI stacked section we observe a dome-like structure with a peak at around 13 m
4 to 17 m horizontal distance (Figure 5b). Indication of such a structure is faint in the
5 CRSS section (Figure 5a). This structure is due to stacking of the surface waves that
6 remained after top muting. The following reasons support this interpretation. First,
7 compared to the raw CRSS shot gathers, reverberating surface waves are accentuated
8 in the raw shot gathers obtained from SI applied to the CRSS data (Figure 4). After top
9 muting, the surface waves are still present more in the SI shot gathers than in the
10 CRSS shot gathers, and these surface waves stack up to produce this dome-like
11 structure, more prominently in the SI stacked section than in the CRSS stacked
12 section. Second, when the surface waves in the CRSS data are greatly suppressed by
13 adaptive subtraction, the stacked section shows no more indication of such dome-like
14 structure (Figure 10b). Third, the frequency content of the dome structure is relatively
15 low and suggestive of ground rolls (see also Figures 4b, 4d and 8b). Finally, in our data
16 acquisition, the geophones were fixed and only the source moved. The CMP fold
17 reaches its maximum at 13.5 m lateral distance and then stays constant at 24 m till
18 18.25 m lateral distance for the CRSS data, whereas it reaches a maximum of 48
19 traces at 15.75 m for the SI data. On both sides of this distance range, the fold
20 gradually decreases (Figure 5). Note that the peak of the dome-like structure is located
21 around 13-17 m distance range (Figure 5b). Both positive and negative offsets in the
22 CMP gather contain the remaining surface waves which stack up at an earlier time.
23 Outside this lateral distance range, the positive and negative offsets are not equal and
24 this inequality increases as we go farther from the above distance range. Accordingly,
25 the result of stacking of the remaining surface waves in the positive and negative
26 offsets gradually changes to create the flank of the dome-like structure.

27 Such a dome-like structural artefact due to stacking of surface waves can be avoided in
28 case the data are acquired using the usual roll-along spread. Then the maximum CMP
29 fold and distribution of source-receiver offset will remain constant over many CMPs.
30 But in that case, the surface waves will stack up to produce an artifact which will
31 appear like a flat, laterally continuous reflector. Because the reverberating surface
32 waves are stronger in the SI data, this is more of a problem in case of SI imaging. Our
33 results indicate that precaution is needed during acquisition and interpretation, in case
34 SI is applied to CRSS data. The strong reverberation of surface waves in case of SI is
35 possibly due to the limitation in the available frequency bandwidth and/or the very near-
36 surface scattering.

1 If a scatterer is present very close to the surface, SI will reveal its presence through
2 retrieval of an event with opposite (positive and negative) linear moveouts at a place of
3 no virtual source. Such an event is visible in Figure 8b close to time zero at
4 approximately 16 m lateral distance. This scatterer will also be imaged in the stacked
5 section, if the event is not suppressed during NMO stacking targeted at imaging the
6 layer boundaries. Additionally, the increased stacking power of SI will make this event
7 stronger compared to CRSS section. In CMP stacking we use the RMS velocity field
8 corresponding to the continuous reflection horizons, and as a result the scatterers are
9 not flattened. As the SI data have a higher number of traces compared to the CRSS
10 data, the imaging of the apex of the scatterers is improved in the SI stacked sections,
11 which was also illustrated in Konstantaki et al. (2013).

12 We use a trace-stacking procedure for imaging after application of SI. This accounts for
13 single scattering. When multiple scattering is present, then the imaging in depth can be
14 improved using advanced imaging conditions incorporated in prestack depth migration
15 (Fleury and Vasconcelos, 2012; Vasconcelos et al., 2012; Ravasi and Curtis, 2013). In
16 addition, we use 2D approximation for the seismic imaging of the scatterers. However,
17 signals from scatterers located in the 3D surrounding of our line are also recorded.
18 Thus, some of the scatterers we are imaging might not be exactly situated under our
19 2D seismic line. On the other hand, scattering from the 3D environment helps to
20 illuminate our receivers better and thus aids in suppressing artifacts. For the AS
21 results, the presence of 3D ambient noise can be an explanation why the filter did not
22 sufficiently remove all surface-wave energy.

23 **8. CONCLUSIONS**

24
25 We studied the application of seismic interferometry (SI) to the conventional reflection
26 seismic survey (CRSS) field data obtained at a landfill, with the goal to improve the
27 imaging and interpretation of the landfill heterogeneities. We have shown that SI
28 applied to the CRSS data improves the imaging of scatterers inside the landfill. We
29 have also shown that scatterers that are located on or close to a layer interface might
30 not be imaged using the CRSS data, but can be imaged using the retrieved SI data.
31 Due to the coarser spatial sampling of the source in the CRSS data, the scatterers
32 might be imaged at a slightly later time/depth. Because the SI-retrieved data have a
33 denser spatial sampling, the chance of imaging the scatterers at their correct
34 time/depth is greater. During the processing of CRSS data, muting of the earlier times
35 might cause shallower scatterers not to be imaged. Such scatterers would still be

1 imaged using the SI-retrieved data. We investigated the efficiency of SI surface-wave
2 prediction and adaptive subtraction from the original CRSS data on landfill. We showed
3 that the obtained adaptively-subtracted (AS) data result in an improved image of the
4 reflectors inside the landfill body. The integrated interpretation of the CRSS, SI and AS
5 data improved the understanding of the landfill's subsurface. The three velocity fields
6 provide complementary information and they may help distinguish the high-density
7 areas that are responsible for the preferential flow paths that occur inside a landfill.
8 This can provide useful information for designing the treatment technologies, for the
9 prediction of the emission potentials, and for assessing the temporal changes in the
10 landfill body.

11 **ACKNOWLEDGEMENTS**

12
13 This research is supported by the *Dutch Technology Foundation (STW)* under the
14 project number 11035. The research of Deyan Draganov is supported by the *Division*
15 *for Earth and Life Sciences (ALW)* with financial aid from the *Netherlands Organization*
16 *for Scientific Research (NWO)*. Seismic data are processed using Seismic Unix and the
17 software package RadExPro[®]. Many thanks to Alber Hemstede, Michael Afanasyev,
18 Shirish Baviskar, Andre van Turnhout, Asiya Kudarova and Andiry Bun for their help in
19 the acquisition of field data. We thank two anonymous reviewers for their constructive
20 comments.

21 **REFERENCES**

- 22 Brouwer J., Ghose R., Helbig K. and Nijhof V., 1997. The improvement of geotechnical
23 subsurface models through the application of S-wave reflection seismic
24 exploration. 3rd Annual Meeting, EEGS, Extended Abstracts, 103-106.
- 25 Campillo M. and Paul A., 2003. Long-range correlations in the diffuse seismic coda.
26 *Science* 299. doi:10.1126/science.1078551
- 27 Dong S., He R. and Schuster T., 2006. Interferometric prediction and least-squares
28 subtraction of surface waves. SEG Technical Program Expanded Abstracts
29 2006, 2783-2786.
- 30 Draganov D., Wapenaar C.P.A., Mulder W., Singer J. and Verdel A., 2007. Retrieval of
31 reflections from seismic background-noise measurements. *Geophysical*
32 *Research Letters* 34. doi:10.1029/2006GL028735

- 1 Draganov D., Campman X., Thorbecke J., Verdel A. and Wapenaar C.P.A., 2009.
2 Reflection images from ambient seismic noise. *Geophysics* 74, A63-A67.
3 doi:10.1190/1.3193529
- 4 Draganov D., Heller K. and Ghose R., 2012. Monitoring CO₂ storage using ghost
5 reflections retrieved from seismic interferometry. *International Journal of*
6 *Greenhouse Gas Control* 11S, S35-S46. doi:10.1016/j.ijggc.2012.07.026
- 7 Fleury C. and Vasconcelos I., 2012. Imaging condition for nonlinear scattering-based
8 imaging. Estimate of power loss in scattering. *Geophysics* 77, S1-S18.
9 doi:10.1190/geo2011-0135.1
- 10 Ghose R., 2002. High-frequency shear wave reflections from shallow subsoil layers
11 using a vibrator source: Sweep cross-correlation versus deconvolution with
12 groundforce derivative. 72nd Annual International Meeting, SEG, Expanded
13 Abstracts, 1408-1411.
- 14 Ghose R., 2003. High-frequency shear-wave reflections to monitor lateral variations in
15 soil, supplementing downhole geotechnical test, in: J. Saveur (Ed.), *Reclaiming*
16 *the Underground Space*. Proc. ITA World Tunneling Congress, Amsterdam,
17 The Netherlands, Swets & Zeitlinger, Lisse, 827-833.
- 18 Ghose R., 2012. A microelectromechanical system digital 3C array seismic cone
19 penetrometer. *Geophysics* 77, WA99-WA107. doi:10.1190/GEO2011-0266.1
- 20 Ghose R., Brouwer J. and Nijhof V., 1996. A portable S-wave vibrator for high-
21 resolution imaging of the shallow subsurface. 58th Annual International
22 Conference and Exposition, EAGE, Extended Abstracts, M037.
- 23 Ghose R., Nijhof V., Brouwer J., Matsubara Y., Kaida Y. and Takahashi T., 1998.
24 Shallow to very shallow, high-resolution reflection seismic using a portable
25 vibrator system. *Geophysics* 63, 1048-1056. doi:10.1190/1.444798
- 26 Ghose R. and Goudswaard J., 2004. Integrating S-wave seismic reflection data and
27 cone-penetration-test data using a multiangle multiscale approach. *Geophysics*
28 69, 440-459. doi:10.1190/1.1707064
- 29 Guitton A. and Verschuur D.J., 2004. Adaptive subtraction of multiples using the L₁-
30 norm. *Geophysical Prospecting* 52, 27-38. doi:10.1046/j.1365-
31 2478.2004.00401.x
- 32 Halliday D.F., Curtis A., Robertsson O.A. and van Manen D.-J., 2007. Interferometric
33 surface wave isolation and removal. *Geophysics* 72, A69-A73.
34 doi:10.1190/1.2761967
- 35 Halliday D.F., Curtis A., Vermeer P., Strobbia C., Glushchenko A., van Manen D.-J.
36 and Robertsson O.A., 2010. Interferometric ground-roll removal: Attenuation of

1 scattered surface waves in single-sensor data. *Geophysics* 75, SA15-SA25.
2 doi:10.1190/1.3360948

3 King S. and Curtis A., 2012. Suppressing nonphysical reflections in Green's function
4 estimates using source-receiver interferometry. *Geophysics* 77, Q15-Q25.
5 doi:10.1190/geo2011-0300.1

6 Konstantaki L.A., Draganov D., Heimovaara T. and Ghose R., 2013. Imaging scatterers
7 in landfills using seismic interferometry. *Geophysics* 78, 1-10.
8 doi:10.1190/GEO2013-0099.1

9 Konstantaki L.A., Ghose R., Draganov D., Diaferia G. and Heimovaara T., 2015.
10 Characterization of a heterogeneous landfill using seismic and electrical
11 resistivity data. *Geophysics* 80, 1-13, doi:10.1190/GEO2014-0263.1

12 McDougall J.R. and Fleming I.R., 2013. Hydro-bio-mechanical modelling of filling and
13 post closure landfill behaviour - a case study. HPM5 Fifth international
14 workshop on hydro-physico-mechanics of landfills, Edinburgh, 77-88.

15 Ravasi M. and Curtis A., 2013. Nonlinear scattering based imaging in elastic media:
16 Theory, theorems and imaging conditions. *Geophysics* 78, S137-S155.
17 doi:10.1190/geo2012-0286.1

18 Scharff H., 2005. Ideas and intentions of the Dutch sustainable landfill research
19 program. Presented at the International Seminar and Workshop "The
20 Sustainable Landfilling" Abbey of Praglia, Padua, Italy.

21 Schuster G.T., 2001. Theory of daylight interferometric imaging: Tutorial. 63rd Annual
22 International Conference and Exhibition, EAGE, Extended Abstracts, A32.

23 Schuster G.T., Yu J., Sheng J. and Rickett J., 2004. Interferometric/daylight seismic
24 imaging. *Geophysical Journal International* 157, 838-852. doi:10.1111/j.1365-
25 246X.2004.02251.x

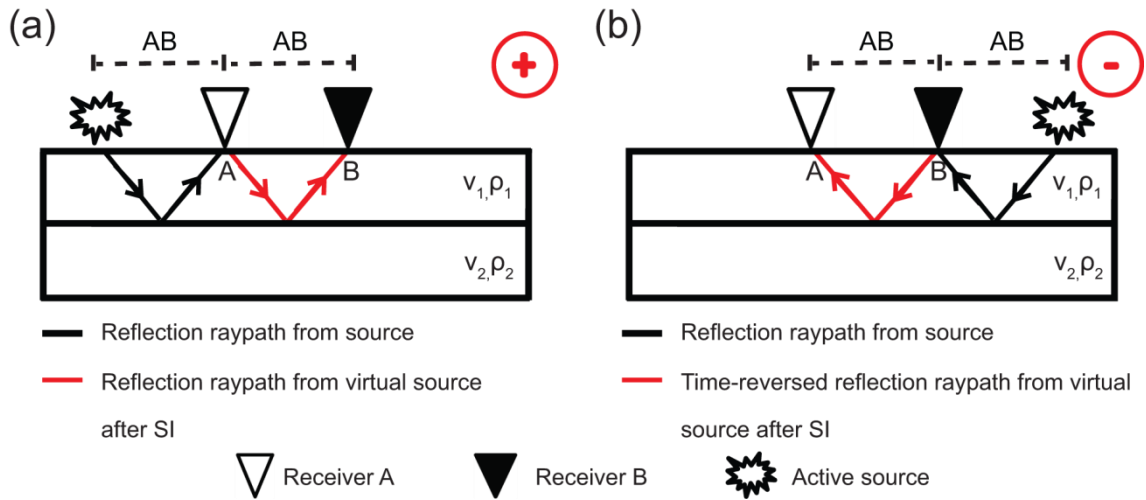
26 Shapiro N.M. and Campillo M., 2004. Emergence of broadband Raleigh waves from
27 correlations of the ambient seismic noise. *Geophysical Research Letters* 31,
28 L07614. doi:10.1029/2004GL019491

29 Snieder R., 2004. Extracting the Green's function from the correlation of coda waves: A
30 derivation based on stationary phase. *Physical Review E* 69, 0466610, doi:
31 10.1103/PhysRevE.69.046610

32 Snieder R., Wapenaar C.P.A. and Lerner K., 2006. Spurious multiples in seismic
33 interferometry of primaries. *Geophysics* 71, S111-S1124.
34 doi:10.1190/1.2211507

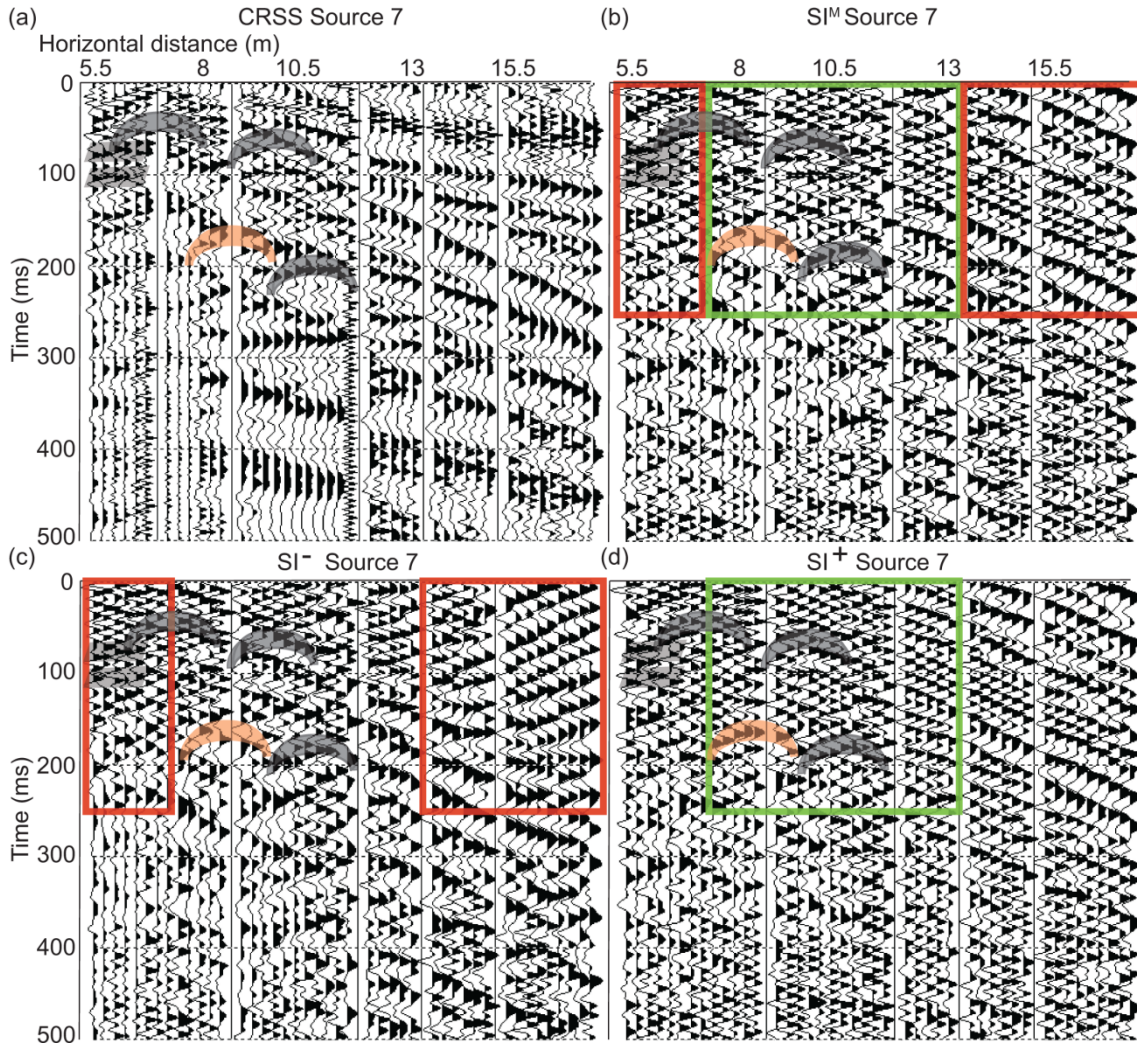
35 Thorbecke J. and Draganov D., 2011. Finite-difference modeling experiments for
36 seismic interferometry. *Geophysics* 76, H1-H18. doi:10.1190/geo2010-0039.1

- 1 van Manen D.-J., Robertsson O.A. and Curtis A., 2005. Modeling of wave propagation
2 in inhomogeneous media. *Physical Review Letters* 94, 164301,
3 doi:10.1103/PhysRevLett.94.164301
- 4 van Vossen W.J., 2010. Sustainable landfilling in the Netherlands: developments,
5 methodologies and experiences. *Österreichische Wasser- und Abfallwirtschaft*
6 62, 141-148. doi:10.1007/s00506-010-0201-6
- 7 van Wijk K., 2006. On estimating the impulse response between receivers in a
8 controlled ultrasonic experiment. *Geophysics* 71, S179-S184.
- 9 Vasconcelos I., Robertsson J., Vassalo M. and van Manen D.-J., 2012. Reverse-time
10 imaging of dual-source 4C marine seismic data using primaries, ghosts and
11 multiples. 74th Annual Conference and Exhibition, EAGE, Extended Abstracts,
12 X045.
- 13 Verschuur D.J., Berkhout A.J. and Wapenaar C.P.A., 1992. Adaptive surface-related
14 multiple elimination. *Geophysics* 57, 1166-1177. doi:10.1190/1.1443330
- 15 Wapenaar C.P.A., 2004. Retrieving the elastodynamic Green's function of an arbitrary
16 inhomogeneous medium by cross correlation. *Physical Review Letters* 93,
17 254301. doi:10.1103/PhysRevLett.93.254301
- 18 Wapenaar C.P.A., 2006. Green's function retrieval by cross-correlation in case of one-
19 sided illumination. *Geophysical Research Letters* 33, L19304.
20 doi:10.1029/2006GL027747.
- 21 Wapenaar C.P.A., Draganov D., Thorbecke J. and Fokkema J.T., 2002. Theory of
22 acoustic daylight imaging revisited. 72nd Annual International Meeting, SEG,
23 Expanded Abstracts, 2269-2272.
- 24 Wapenaar C.P.A. and Fokkema J., 2006. Green's function representations for seismic
25 interferometry. *Geophysics* 71, SI33-S146. doi:10.1190/1.2213955
- 26 Wapenaar C.P.A., Draganov, D., Snieder, R., Campman, X. and Verdel, A., 2010a.
27 Tutorial on seismic interferometry: Part 1 - Basic principles and applications.
28 *Geophysics* 75, 75A195-75A209, doi:10.1190/1.3457445
- 29 Wapenaar C.P.A., Slob E., Snieder R. and Curtis A., 2010b. Tutorial on seismic
30 interferometry: Part 2 - Underlying theory and new advances. *Geophysics* 75,
31 75A211-75A227. doi:10.1190/1.3463440
- 32 White J.K., Robinson J. and Ren Q., 2004. Modelling the biochemical degradation of
33 solid waste in landfills. *Waste Management* 24, 227-240.
34 doi:10.1016/j.wasman.2003.11.009
- 35 Zhu J., Lines L.R. and Gray S.H., 1998. Smiles and frowns in migration/velocity
36 analysis. *Geophysics* 63, 1200-1209. doi:10.1190/1.1444420



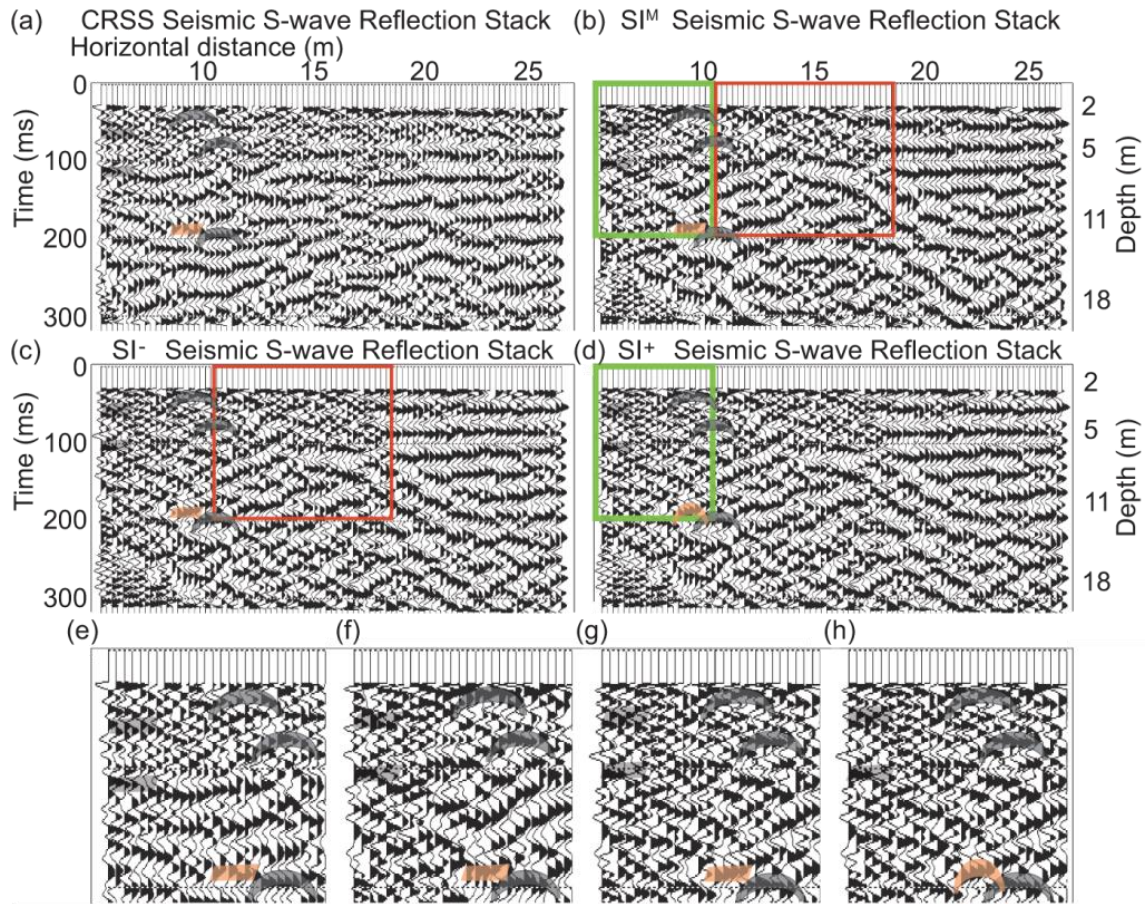
1
 2 **Figure 1:** Explanation of retrieval of a reflection at B from a virtual source at A. The
 3 active source is at distance AB from A or from B. (a) When the active source is to the
 4 left of A, the reflection is retrieved at positive times. (b) When the active source is to the
 5 right of B, the reflection would be retrieved at negative times. The symbols v and ρ
 6 denote velocity and density, respectively.

7
 8
 9
 10
 11
 12
 13
 14
 15
 16
 17
 18
 19
 20
 21
 22
 23
 24
 25
 26
 27



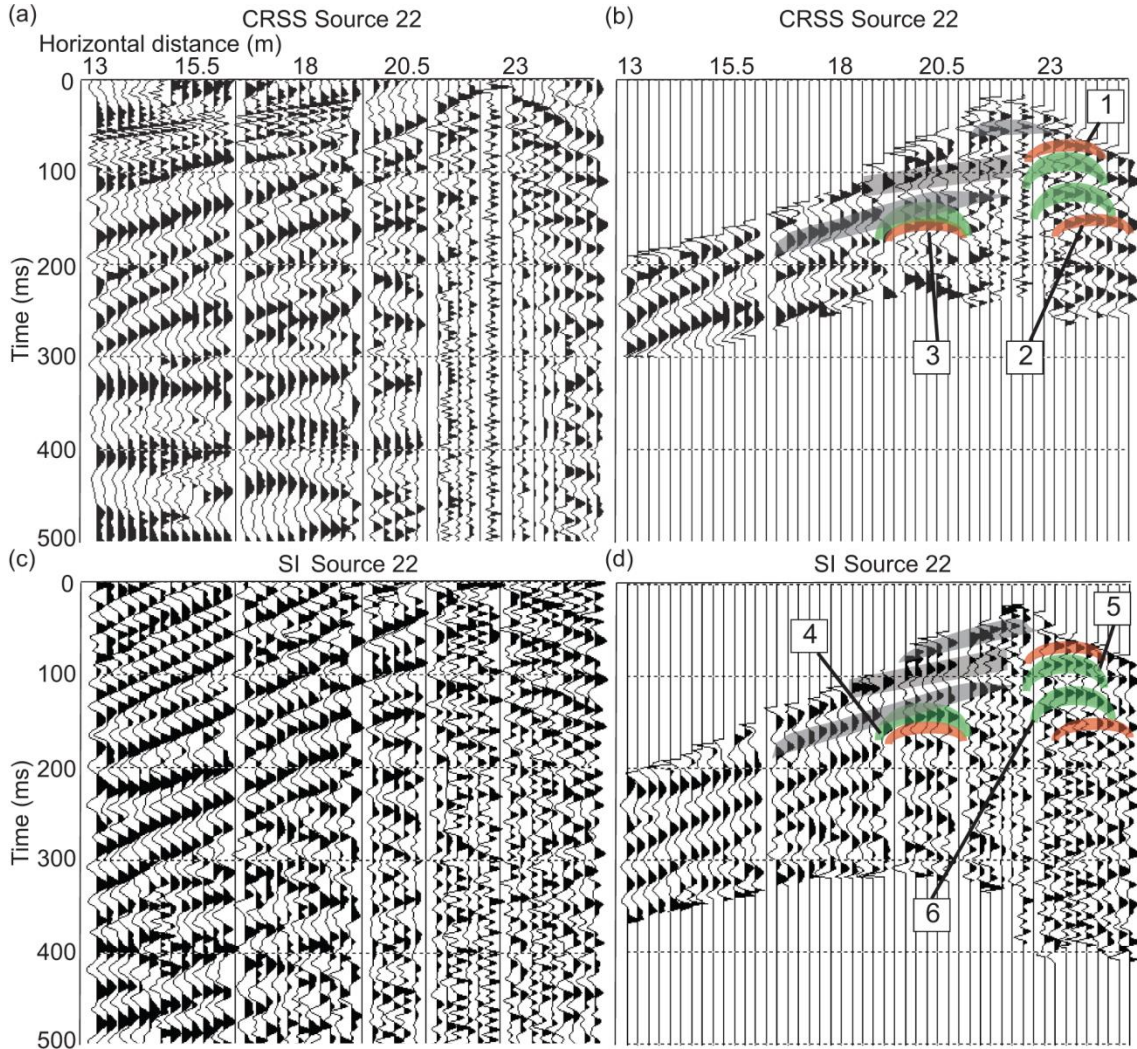
1
 2 **Figure 2:** Raw shot gather for a source located at horizontal distance 7 m, obtained
 3 from (a) conventional reflection seismic survey (CRSS), (b) seismic interferometry (SI)
 4 using the mixed-traces approach (SI^M), (c) SI taking only the negative times (SI^-), and
 5 (d) SI taking only the positive times (SI^+). The green rectangle shows areas of
 6 improvement in SI^M over SI^+ , the red rectangles show areas of improvement in SI^M over
 7 SI^- . The grey-shaded areas and hyperbolas show reflection and scattering events,
 8 respectively. The orange hyperbola indicates an artifact in SI^+ . Note that we apply a
 9 different bandpass filter to the SI results (Figures 2b,c,d) compared to the CRSS result
 10 (Figure 2a).

11
 12
 13
 14
 15
 16



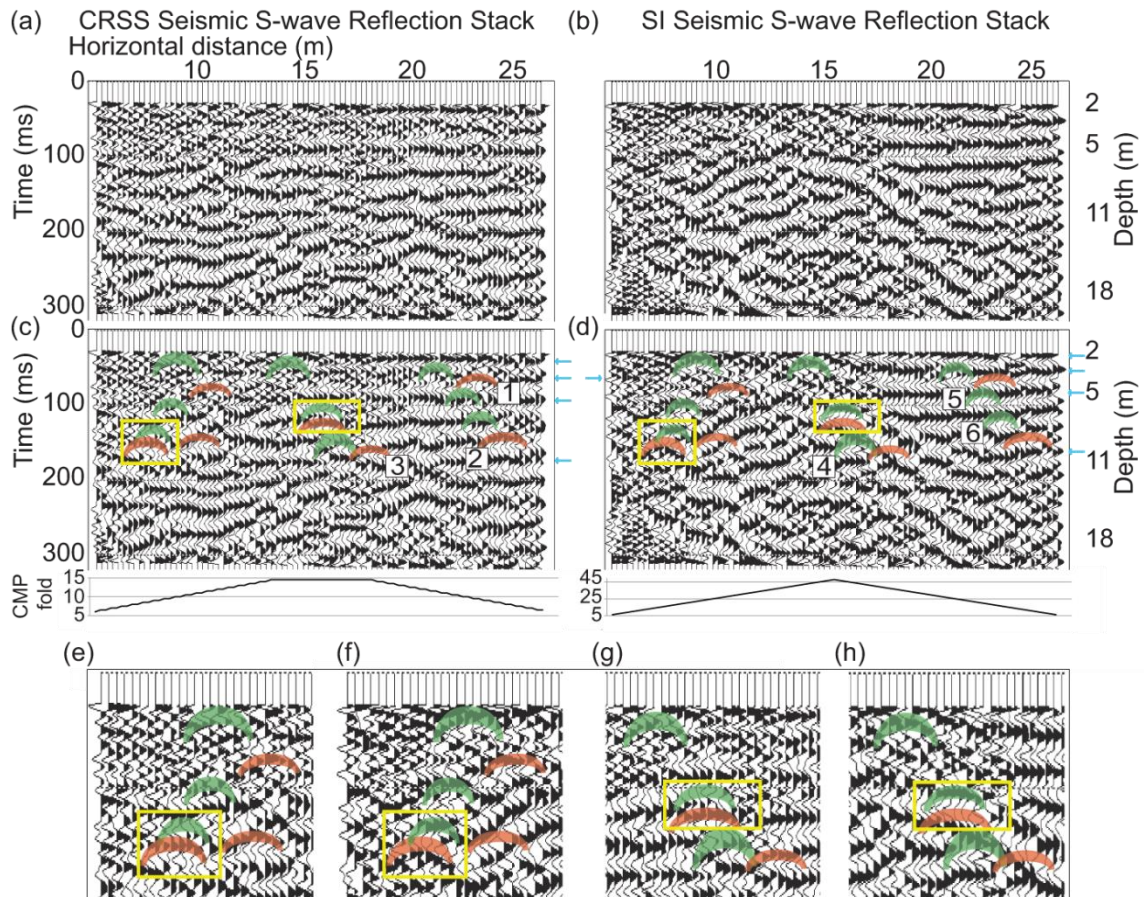
1
2 **Figure 3:** Stacked section obtained from (a) conventional reflection seismic survey
3 (CRSS), (b) seismic interferometry (SI) using the mixed-traces approach (SI^M), (c), SI
4 taking only the negative times (SI^-) and, (d) SI taking only the positive times (SI^+). (e)
5 enlarged area showing the scatterers in (a), (f) enlarged area showing the scatterers in
6 (b), (g) enlarged area showing the scatterers in (c), (h) enlarged area showing the
7 scatterers in (d). The green rectangle shows the area of improvement in SI^M over SI^+ ,
8 the red rectangle shows the area of improvement of SI^M over SI^- . The grey-shaded
9 areas and hyperbolas mark some reflections and scatterers, respectively. The orange
10 hyperbola indicates an artifact in SI^+ . The dome-like structure in the middle,
11 accentuated in the SI sections, is due to the remaining surface waves and the laterally
12 varying positive and negative offsets due to split-spread data acquisition with a fixed
13 receiver array, which will be explained further in the Discussion section.

14
15
16
17
18



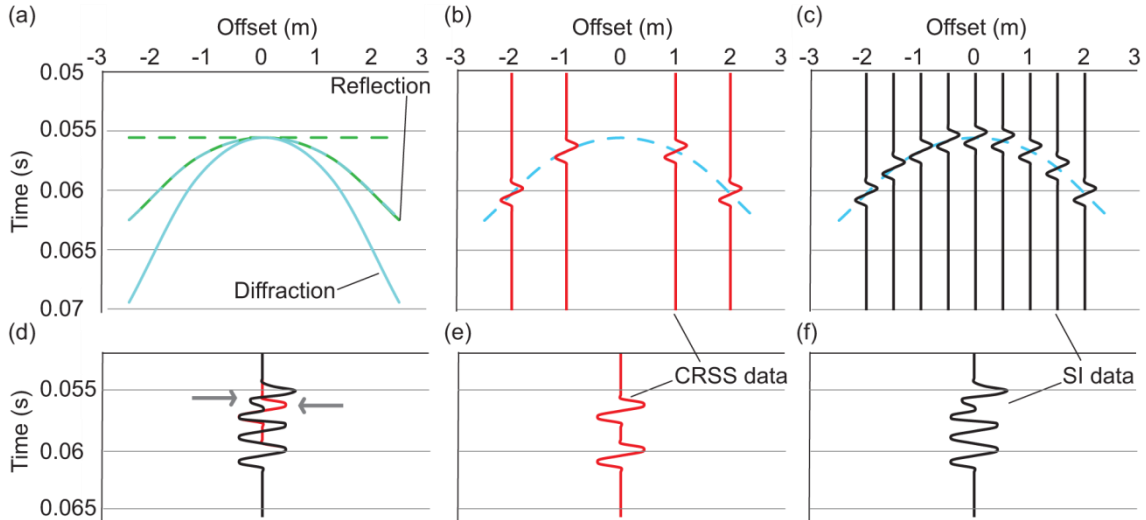
1 **Figure 4:** (a) Raw and (b) processed shot gather obtained from conventional reflection
 2 seismic survey (CRSS) for a source located at horizontal distance 22 m. (c) Raw and
 3 (d) processed shot gather obtained from seismic interferometry (SI) applied to the
 4 CRSS data, for a virtual source located at horizontal distance 22 m. The red
 5 hyperbolas show scattering events interpreted on the CRSS data, whereas the green
 6 hyperbolas mark scattering events interpreted on the SI data. The grey-shaded areas
 7 indicate mostly reflections.
 8

9
 10
 11
 12
 13
 14
 15
 16



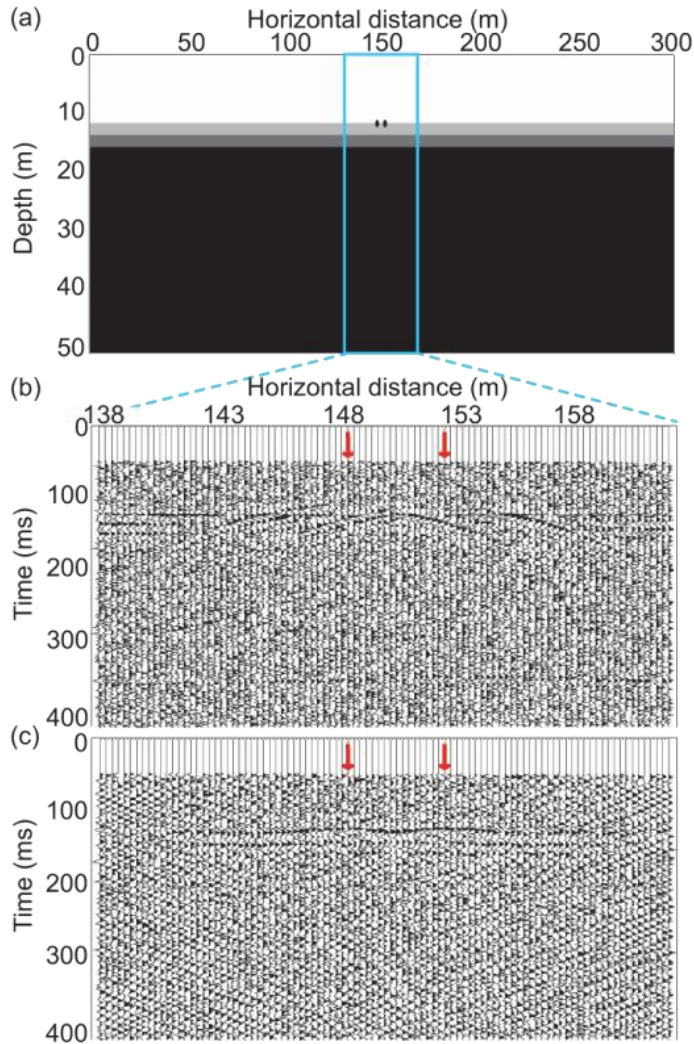
1
2 **Figure 5:** Stacked section obtained from (a) conventional reflection seismic survey
3 (CRSS) and, (b) seismic interferometry (SI) with the mixed-traces approach applied to
4 the CRSS data. (c) and (d) show the interpretation from (a) and (b), respectively, (e)
5 enlarged area showing the scatterers in the left side of (c), (f) enlarged area showing
6 the scatterers in the left side of (d), (g) enlarged area showing the scatterers in the
7 middle of (c), (h) enlarged area showing the scatterers in the middle of (d). The red
8 hyperbolas show scatterers interpreted on the CRSS data, whereas the green
9 hyperbolas show scatterers interpreted on the SI data. The numbers correspond to the
10 scattering events shown in Figure 4. The yellow rectangles illustrate examples of
11 opposite-polarity effect. The blue arrows point to reflectors. The CMP fold distribution is
12 shown in the lower part. Note that the peak of the dome-like structure, more prominent
13 in the SI reflection stack (b), is located in the lateral distance range which corresponds
14 to the maximum CMP fold.

15
16
17
18



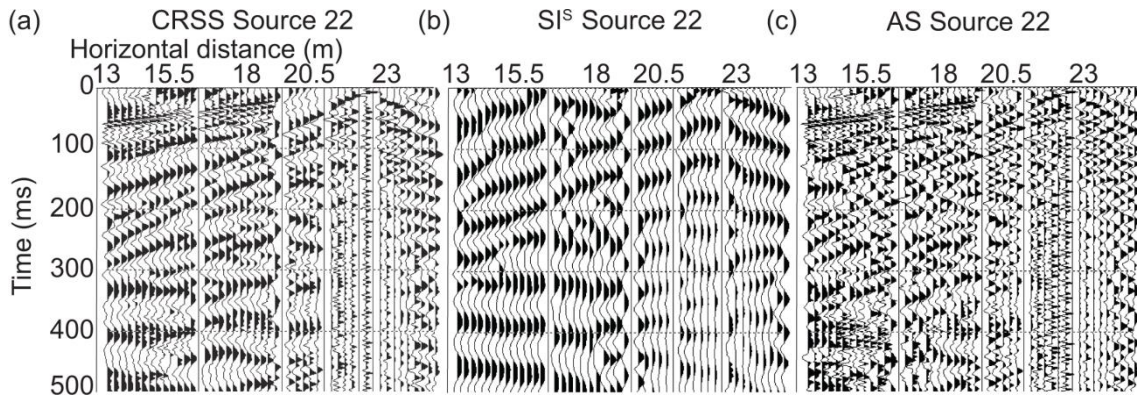
1 **Figure 6:** (a) Reflection and diffraction hyperbolas (solid lines) and their alignment after
 2 normal moveout (NMO) correction (dashed lines) using the root-mean square velocity
 3 of the reflection event. (b) Diffraction event in the common-midpoint (CMP) gather of
 4 conventional reflection seismic survey (CRSS) and, (c) diffraction event in the CMP
 5 gather of seismic interferometry (SI). (d) Comparison of stacked CRSS (red) and SI
 6 (black) traces, (e) stacked CRSS trace only, (f) stacked SI trace only. The grey arrows
 7 in (d) mark the opposite-polarity effect.
 8

9
 10
 11
 12
 13
 14
 15
 16
 17
 18
 19
 20
 21
 22
 23
 24
 25



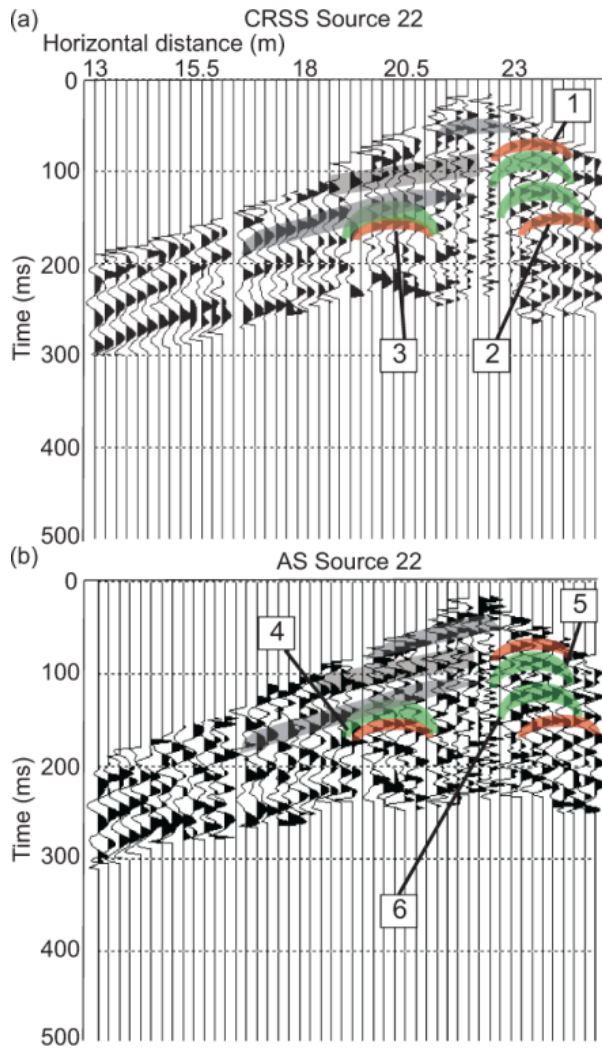
1
 2 **Figure 7:** (a) Velocity model for forward modelling of a situation where two scatterers
 3 are located at the boundary between the two layers. Synthetic stacked section obtained
 4 using the (b) conventional reflection seismic survey (CRSS) data and (c) data retrieved
 5 by application of seismic interferometry to the CRSS data. The red arrows indicate the
 6 location of the scatterers.

7
 8
 9
 10
 11
 12
 13
 14
 15
 16



1 **Figure 8:** Shot gather for source located at horizontal distance 22 m obtained from (a)
 2 conventional reflection seismic survey (CRSS), (b) seismic interferometry focused
 3 towards retrieving primarily the surface waves, and (c) CRSS after adaptive subtraction
 4 of the retrieved surface waves, which is the subtraction of the gather in (b) from that in
 5 (a).
 6

7
 8
 9
 10
 11
 12
 13
 14
 15
 16
 17
 18
 19
 20
 21
 22
 23
 24
 25
 26
 27
 28
 29



1
 2 **Figure 9:** The shot gather (a) from Figure 8a and (b) from Figure 8c after processing
 3 (top and bottom muting). The red hyperbolas show the scattering events interpreted on
 4 CRSS data, whereas the green hyperbolas mark the same events interpreted on the SI
 5 data. The grey-shaded areas indicate primarily reflections.

6
 7
 8
 9
 10
 11
 12
 13
 14
 15

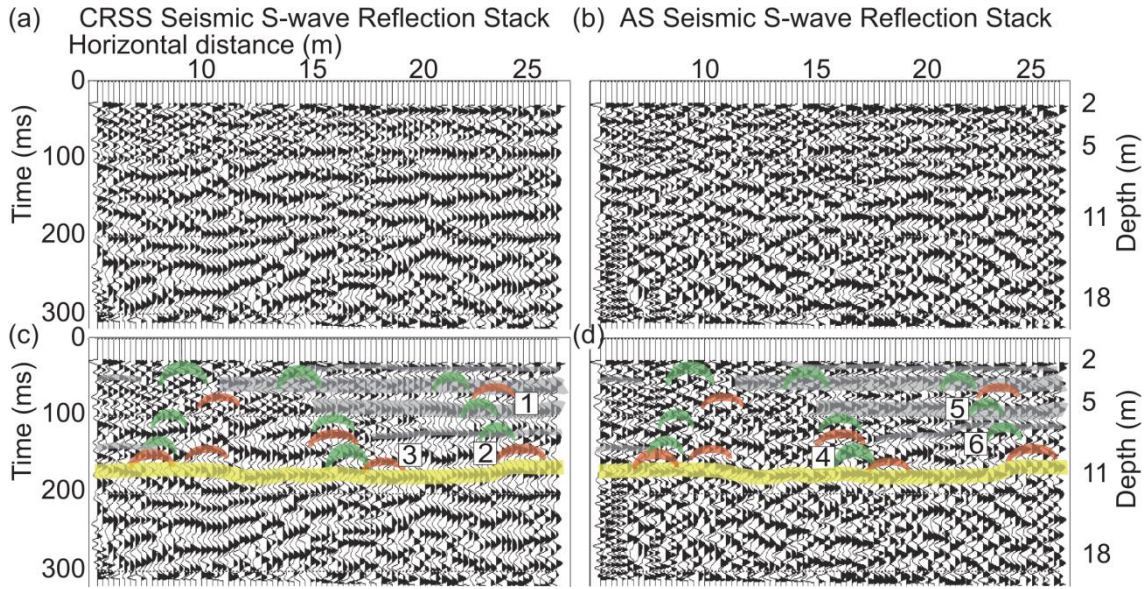
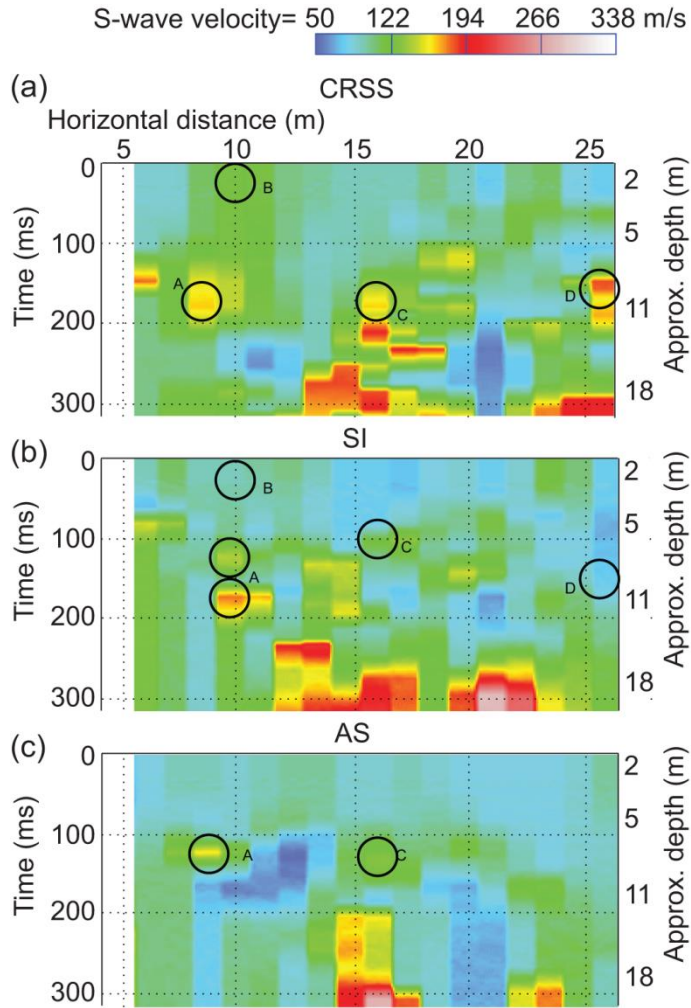


Figure 10: Stacked section obtained from (a) conventional reflection seismic survey (CRSS) and, (b) adaptive subtraction (AS) of surface waves. Interpreted stacked section (c) of CRSS and (d) of AS. The red hyperbolas indicate scatterers interpreted on the CRSS data, whereas the green hyperbolas indicate scatterers interpreted on the SI data. The numbers correspond to scattering events shown in Figure 9. The grey-shaded areas indicate reflectors (layer boundaries). The yellow line indicates the interpreted landfill bottom.

9
 10
 11
 12
 13
 14
 15
 16
 17
 18
 19
 20
 21
 22



1
2 **Figure 11:** S-wave interval velocity field obtained from (a) conventional reflection
3 seismic survey (CRSS) data, (b) seismic interferometry (SI) data and, (c) data after
4 adaptive subtraction (AS) of surface waves. The circles and capital letters indicate
5 areas where differences in the velocity fields among the three fields are observed.
6